Magnetic properties of the magnetoelectric $Al_{2−x}Fe_xO_3$ ($x = 0.8, 0.9$ and 1)

M Pissas, D Stamopoulos, Y Sanakis and A Simopoulos

Institute of Materials Science, NCSR, Demokritos, 15310 Aghia Paraskevi, Athens, Greece

Abstract
By using x-ray diffraction, magnetization and Mössbauer spectroscopy techniques we have
studied the magnetoelectric $Al_{2−x}Fe_xO_3$ ($x = 0.8, 0.9$ and 1.0) compound. Ac-susceptibility
and magnetization measurements revealed magnetic transitions at $T_N = 180, 210$ and 260 K for
$x = 0.8, 0.9$ and 1.0 respectively, that can be attributed to the Néel temperatures of
ferrimagnetic to paramagnetic phase transition for all samples. Mössbauer spectra for the three
samples were recorded between 4.2 and 295 K. Above the Néel temperature the paramagnetic
spectra can be analyzed by three quadrupole doublets associated with the octahedral Fe1, Fe2
and Fe4 sites. The values of the hyperfine parameters show that iron ions are in the high spin
Fe^{3+} state. The spectrum area of the doublet with larger quadrupole splitting increases with x,
and in combination with x-ray diffraction results it can be attributed to the iron which occupies
the Fe4 site. Below $T_N(x)$ the Mössbauer spectra are magnetically split and at $T = 4.2$ K
consist of six broad lines, indicating either a hyperfine magnetic field distribution ($P(H_{hyp})$) or
that the three octahedral sites give three unresolved sextets. The most probable value of H_{hyp}
(the maximum value of $P(H_{hyp})$) follows a power law indicative of a second order transition, in
agreement with ac-susceptibility and magnetization measurements. The width of $P(H_{hyp})$
increases drastically toward low hyperfine magnetic fields as temperature increases. In addition,
an appreciable percentage of the iron nuclei sense a hyperfine field with values in the interval
$[0, H_{max}]$. This behavior can be explained by assuming that several magnetic sites with different
superexchange parameters exist.

(Some figures in this article are in colour only in the electronic version)

1. Introduction

Numerous studies in antiferromagnetic/ferromagnetic and ferroelectric materials show that magnetism and ferroelectricity are two antagonistic properties [1, 2]. A plausible explanation has been given recently [2, 3] based on the Hund's rule, where in an open 3d shell the spins have the tendency to be parallel. This mechanism is opposite to the strong covalent bonding needed for ferroelectricity. Magnetoelectricity can phenomenologically be described [4] with the help of the additional term $\Phi_{m−e} = − \sum_{ij} \alpha_{ik} E_i H_k$, in the thermodynamic potential, describing the magnetic and electric energy of the crystal. Here α_{ij} is the magnetoelectric tensor, **E** and **H** the electric and magnetic fields. Magnetoelectric compounds are very rare since special requirements are necessary. In order for magnetoelectric tensors to have non-zero values, the inversion center should be combined with the operator which reverses all currents (IR) [4]. In these materials

magnetic and electric properties are coupled so that (i) for $H = 0$ the magnetic moment responds to an applied electric field ($M_k = \alpha_{ik} E_i$) and (ii) for $E = 0$ the electric polarization can change with a magnetic field ($P_i = \alpha_{ik} H_k$) as well. Although several studies exist from the early 1960s, the exact microscopic explanation of the magnetoelectric effect still has not been achieved, also corroborated from the rare existence of magnetoelectric compounds. One of them, known from the 1960s, with high anisotropic magnetic properties, is the orthorhombic form of the mixed $Al_{2−x}Fe_xO_3$ compound. Solid state reaction of α-Fe_2O_3 and α-Al_2O_3 in air produces solid solution compounds α-$Al_{2−x}Fe_xO_3$ with rhombohedral structure. If the reaction of samples with nominal stoichiometry $Al_{2−x}Fe_xO_3$, ($0.6 \leqslant x \leqslant 1.35$) takes place at high temperature under pure oxygen atmosphere, then the reaction product is a compound with orthorhombic structure, which is piezoelectric and ferrimagnetic. This compound was discovered by Richardson *et al* [5] when they

heated a mixture consisting of Fe_2O_3 and Al_2O_3 in oxygen at 1400 °C.

Figure 1 shows the crystal structure of the orthorhombic $AlFeO_3$ compound. In an ideal situation it can be considered as a layered structure consisting of three cation layers stacked along the *c*-axis. The first layer is occupied by regular AlO_3 tetrahedra, the second by distorted FeO_6 octahedra and the third by distorted FeO_6 and AlO_6 octahedra. $Al_{2-x}Fe_xO_3$ and its isostructural $Ga_{2-x}Fe_xO_3$ compound attracted considerable research interest in the 1960s [6–20]. Nowadays the research interest for the magnetoelectric compounds has been rekindled [2, 21–24], mainly due to the report of Kimura *et al* [25] on the existence of the magnetoelectric effect in the frustrated-spin $TbMnO_3$ compound. In the case of manganites (e.g. $TbMnO_3$) the magnetoelectric effect is believed to emanate from 'strong bond anisotropy between neighboring ions, induced by orbital ordering. An applied magnetic field modifies the magnetic structure by reducing the exchange energy. In order for the system to compensate for this energy change a lattice distortion is induced which in turn induces electric polarization' [22].

In the present paper we report on crystal and magnetic properties of polycrystalline $Al_{2-x}Fe_xO_3$ ($x = 0.8, 0.9$ and 1) samples using x-ray diffraction, magnetization, ac-susceptibility and Mössbauer measurements. Rietveld refinements showed that the majority of the samples consisted of orthorhombic form, with cell constant increasing with iron content. No structural anomaly is detected on cooling through the Néel temperature, indicating that the magnetic transition is not related to the ferroelectricity, which is an endogenous property related to the non-centrosymmetric crystal structure. The magnetization and ac-susceptibility measurements can be interpreted supposing that the $Al_{2-x}Fe_xO_3$ compound is a ferrimagnet with strong uniaxial anisotropy. The Mössbauer spectra show that iron occupies with aluminum exclusively the octahedral sites, which in turn produce the ferrimagnetic moment.

2. Experimental details

Samples with nominal composition $Al_{2-x}Fe_xO_3$ ($x = 0.8, 0.9$ and 1) were prepared by the standard solid state reaction method using a stoichiometric mixture of Al_2O_3 and Fe_2O_3. If the reaction takes place in air atmosphere we get as a final product a mixture of Al_2O_3 and Fe_2O_3. The same occurs if the heating occurs in oxygen atmosphere but for $T < 1350$ °C. Interestingly, in order to prepare the orthorhombic form of the $Al_{2-x}Fe_xO_3$ compound it is absolutely necessary for the reaction to take place in a narrow temperature window (1350–1395 °C) under pure oxygen atmosphere in agreement with [6, 7]. X-ray powder diffraction (XRD) data were collected with a D500 Siemens diffractometer, using Cu Kα radiation. High-resolution synchrotron x-ray powder diffraction (SXRD) patterns were collected with the multi-detector powder diffractometer on the ID31 beamline at the ESRF (Grenoble, France) in Debye–Scherrer (transmission) configuration. Powder samples were sealed in thin-wall borosilicate glass capillaries ($d = 0.5$ mm), inserted in a
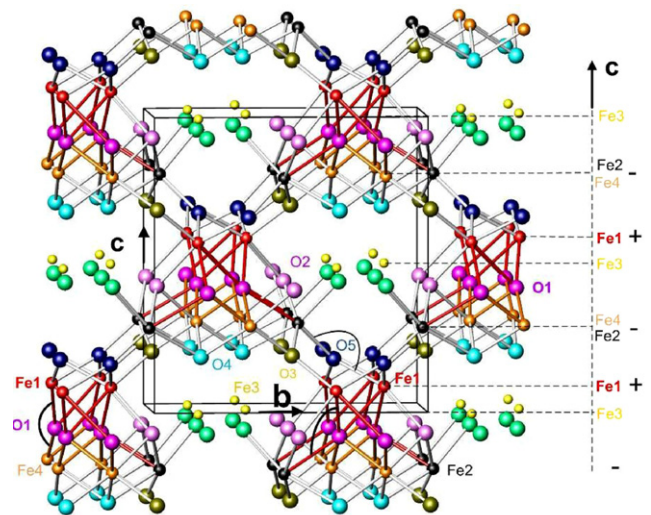

Figure 1. Crystal structure of the orthorhombic $Al_{2-x}Fe_xO_3$ compound (space group $Pna2_1$). There are four cation and six oxygen sites labeled Fe1–Fe4 and O1–O6, respectively. The Fe3 and (Fe1, Fe2, Fe4) sites are tetrahedrally and octahedrally coordinated, respectively. For low iron concentration Fe1 and Fe2 are commonly occupied by aluminum and iron. For higher *x* iron is substituted for aluminum at Fe4 sites. The Fe3 site is practically occupied by aluminum. The polar axis of the structure is parallel with the *c*-axis. The crystal structure can be considered as a layered structure consisting of alternating cation layers of Fe1 and (Fe2, Fe4) separated from oxygen layers. In the magnetically ordered state the magnetic moments are parallel to the *a*-axis stacked in a $+ - + -$ sequence along the *c*-axis.

continuous-flow cryostat and rotated during data collection. Data were collected at selected temperatures between 5 and 300 K on both cooling and heating with wavelength $\lambda = 0.500\,08$ Å, and were rebinned in the range 4°–60° to a 0.003° step.

DC magnetization measurements were performed in a superconducting quantum interference device (SQUID) magnetometer (Quantum Design). Ac-susceptibility measurements were performed using a physical property measuring system (PPMS, Quantum Design) equipped with ac-susceptibility option. The absorption Mössbauer spectra (MS) were recorded using a conventional constant acceleration spectrometer with a ^{57}Co (Rh) source moving at room temperature, while the absorber was kept fixed in a variable temperature cryostat. The resolution was determined to be $\Gamma/2 = 0.14$ mm s^{-1} using a thin α-Fe foil.

3. X-ray diffraction data

The crystal structure of the orthorhombic $Al_{2-x}Fe_xO_3$ compound has been deduced from the single crystal crystallographic studies of Abrahams and co-workers in the middle of the 1960s [26] on the isostructural $Ga_{2-x}Fe_xO_3$ compound using the non-centrosymmetric space group $Pna2_1$. In addition, the crystal structure of $Ga_{2-x}Fe_xO_3$ has been refined using neutron powder data at several temperatures in the past by Bertaut *et al* [18] and recently by Arina *et al* [23]. Crystal structure data of the $Al_{2-x}Fe_xO_3$ compound are

Figure 2. Rietveld plot of AlFeO$_3$ compound sample at $T = 295$ K measured with synchrotron x-rays ($\lambda = 0.5$ Å) at the ID31 beam line of the ESRF. The observed data points are indicated by open circles, while the calculated and difference patterns are shown by solid lines. The positions of the reflections are indicated by vertical lines below the patterns.

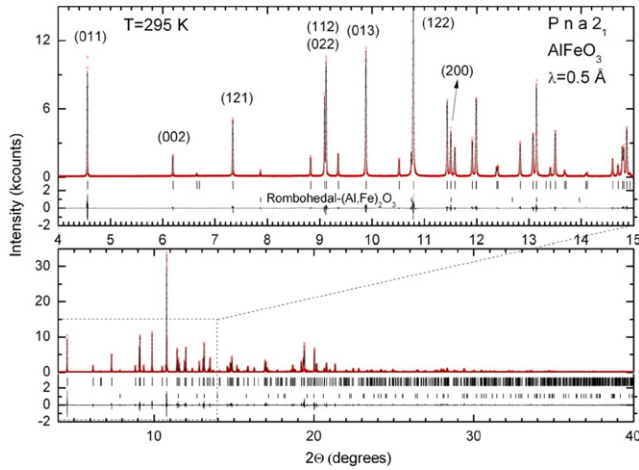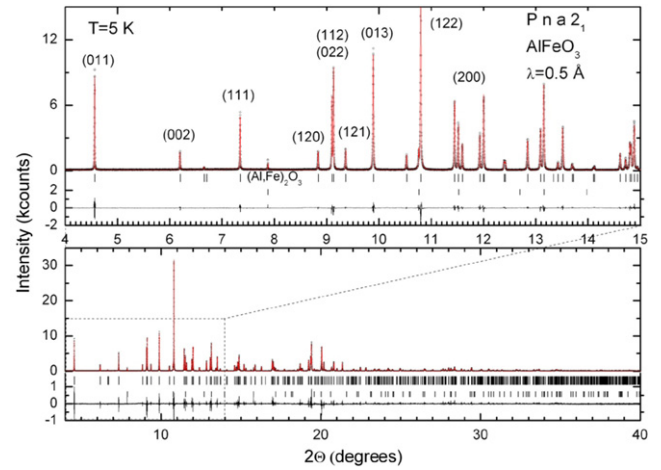**Figure 3.** Rietveld plot of AlFeO$_3$ compound at $T = 5$ K measured with synchrotron x-rays ($\lambda = 0.5$ Å) at the ID31 beam line of the ESRF. The observed data points are indicated by open circles, while the calculated and difference patterns are shown by solid lines. The positions of the reflections are indicated by vertical lines below the patterns.

available only for the $x = 1$ sample originating from the crystal structure refinement of Bouree *et al* [19], based on powder neutron diffraction data. The asymmetry unit includes four cation and six anion sites labeled Fe1, Fe2, Fe3 and Fe4 and O1–O6, respectively. The crystal structure of Al$_{2-x}$Fe$_x$O$_3$ can be considered as a layer structure consisting essentially of three types of cation layers, stacked along the c-axis (see figure 1). The first two layers, with small separation along the c-axis ($\Delta z \sim 0.08c$), include the Fe3 sites (mainly occupied by Al) and the Fe1 sites occupied by both Fe and Al ions. The third layer concerns the Fe2 and Fe4 sites ($\Delta z \sim 0.01c$) also occupied by both Al and Fe ions. The cations in one layer form chains along the a-axis. The cation layers are separated from layers occupied exclusively with oxygen, appropriately arranged in order for the cation polyhedra of Fe1, Fe2 and Fe4 sites to be irregular (non-rigid) octahedra while those of Fe3 are nearly regular tetrahedra.

Our powder x-ray diffraction data at $T = 300$ K were refined using the Rietveld refinement method, with the FULLPROF suite of programs [27], assuming the orthorhombic polar space group $Pna2_1$. As initial crystal structure model we adopted the one reported by Bouree *et al* [19]. Since $Pna2_1$ is a polar space group the z positional parameter of the Fe3 site is kept at zero. Figures 2 and 3 show the Rietveld plots of the Al$_{2-x}$Fe$_x$O$_3$ ($x = 1$) sample at $T = 300$ and 5 K arising from crystal structure refinement of the powder synchrotron x-ray diffraction data measured at ESRF. The lower panels of figures 2 and 3 show the complete pattern, while the upper parts show a zoom in the range 4°–15°. The background is accounted for by linear interpolation between points without the Bragg's peak contribution. As peak shape function we selected the pseudo-Voigt (no 7) function convoluted with the Finger, Cox and Jephcoat function in order to account for the axial divergence [28]. The dependence of the full width at half maximum (FWHM) of the peak profiles on the scattering variable, 2Θ, is given by

equation FWHM $= \sqrt{U \tan^2\theta + V \tan\theta + W} + X \tan\theta + Y/\cos\theta$. Owing to the ultra-high resolution of the ID31 diffractometer we ascertained that the diffraction peaks are characterized by selective peak broadening. Such a type of broadening can be accounted for by using the formalism developed by Stephens [29]. In this model the anisotropic strain broadening effects are phenomenologically attributed to a stochastic distribution of the metric parameter vector $\boldsymbol{\alpha} = (A, B, C, D, E, F)$, determining the inverse square lattice plane spacing $M_{hkl} = 1/d_{hkl}^2 = Ah^2 + Bk^2 + Cl^2 + Dkl + Ehl + Fhk$. In the orthorhombic system the variance $\sigma^2(M_{hkl})$ can be expressed by six independent parameters [29] ($S_{400}, S_{040}, S_{004}, S_{220}, S_{202}, S_{022}$) through the relation $\sigma^2(M_{hkl}) = S_{400}h^4 + S_{040}k^4 + S_{004}l^4 + S_{220}h^2k^2 + S_{202}h^2l^2 + S_{022}k^2l^2$, that can be estimated from the Rietveld refinement. In order to simplify the refinement, we kept the isotropic Gaussian U, V, W and Lorentzian X, Y FWHM parameters zero, and we used the parameter ξ which 'shares' the anisotropic FWHM in the Gaussian $H_G^2 = (1 - \xi)^2 D^2 \tan^2\theta$ and Lorentzian $H_L = \xi D \tan\theta$ parts, where $D^2 = 10^{-8} 8 \ln 2 (180/\pi)^2 \sigma^2(M_{hkl})/M_{hkl}^2$. We must note that the reliability factors have been reduced by approximately half by introducing the Stephens' formalism, in comparison to the results obtained by isotropic line shape parameters.

At the first steps of the refinement we used as free parameters the scale factor, unit cell constants and anisotropic microstructure parameters defining the full width at the half maximum (FWHM), and cation atomic positions Fe1, Fe2, Fe3 and Fe4 sites are supposed to be occupied exclusively by iron and aluminum, respectively. Having attained a reasonable agreement, a close inspection of the low angle part of the difference patterns revealed small diffraction peaks arising from the rhombohedral form of the solid solution Al$_{2-x}$Fe$_x$O$_3$ compound. Based on this, we employ a two phase refinement model. Nevertheless, the amount of the secondary phases was

Table 1. The structural parameters of $Al_{2-x}Fe_xO_3$ ($x = 0.8$, 0.9 and 1.0) at $T = 295$ K as determined from Rietveld refinement based on x-ray diffraction data. The space group $Pna2_1$ (No 33) was used. Numbers in parentheses are statistical errors referring to the last significant digit. The results for the samples with $x = 0.9$ and 1.0 emanate from SXRD data.

Atom	x	y	z	B	N
$x = 0.8$, $a = 4.9650(1)$ Å, $b = 8.5219(1)$ Å, $c = 9.2131(1)$ Å					
Fe1	0.1875(6)	0.1524(4)	0.581(4)	0.41(3)	0.63(1)/0.47(1)
Fe2	0.6688(4)	0.0323(2)	0.798(6)	0.41(3)	0.65(1)/0.35(1)
Fe3	0.1730(8)	0.1529(8)	0.000(0)	0.46(6)	0.0/1.0
Fe4	0.8195(7)	0.1597(3)	0.301(8)	0.50(6)	0.13(1)/0.87(1)
O1	0.987(2)	0.323(1)	0.416(1)	0.74(6)	1.0(0)
O2	0.505(1)	0.489(1)	0.426(1)	0.74(6)	1.0(0)
O3	0.655(2)	1.002(1)	0.200(1)	0.74(6)	1.0(0)
O4	0.151(2)	0.159(1)	0.192(1)	0.74(6)	1.0(0)
O5	0.839(2)	0.164(1)	0.669(1)	0.74(6)	1.0(0)
O6	0.504(2)	0.175(1)	0.940(1)	0.74(6)	1.0(0)
$R_p = 5.8$, $R_{wp} = 8.1$, $R_{exp} = 4.91$, $R_B = 3.2$, $\chi^2 = 2.7$					
$x = 0.9$, $a = 4.9745(1)$ Å, $b = 8.5393(2)$ Å, $c = 9.2311(2)$ Å					
Fe1	0.1833(5)	0.1509(4)	0.5820(4)	1.1(1)	0.66(1)/0.34(1)
Fe2	0.6704(4)	0.0322(2)	0.7990(6)	1.1(1)	0.64(1)/0.35(1)
Fe3	0.1718(7)	0.1537(7)	0.0	1.0(1)	0.03(1)/0.96(1)
Fe4	0.8158(5)	0.1609(3)	0.304(1)	0.6(8)	0.13(1)/0.86(1)
O1	0.9676(5)	0.3237(9)	0.421(1)	1.2(1)	1.0
O2	0.508(1)	0.4909(9)	0.431(1)	1.2(1)	1.0
O3	0.659(2)	1.0042(8)	0.199(1)	1.2(1)	1.0
O4	0.136(1)	0.1678(9)	0.195(1)	1.2(1)	1.0
O5	0.824(2)	0.1718(9)	0.670(1)	1.2(1)	1.0
O6	0.499(2)	0.172(1)	0.942(1)	1.2(1)	1.0
$R_p = 12.4$, $R_{wp} = 16.4$, $R_{exp} = 12.2$, $R_B = 3.6$, $\chi^2 = 1.8$					
$x = 1$, $a = 4.9899(1)$ Å, $b = 8.5670(1)$ Å, $c = 9.2592(1)$ Å					
Fe1	0.1847(2)	0.1513(1)	0.5808(1)	0.73(2)	0.684(4)/0.314(4)
Fe2	0.6709(1)	0.0328(1)	0.7975(2)	0.74(2)	0.673(3)/0.327(3)
Fe3	0.1728(3)	0.1542(2)	0.0	0.95(3)	0.053(2)/0.947(2)
Fe4	0.8156(2)	0.1605(1)	0.3042(2)	0.49(2)	0.183(3)/0.817(3)
O1	0.9824(6)	0.3236(3)	0.4211(4)	1.31(3)	1.0
O2	0.5058(5)	0.4917(3)	0.4290(3)	1.31(3)	1.0
O3	0.6581(6)	1.0037(3)	0.1992(4)	1.31(3)	1.0
O4	0.1448(6)	0.1648(3)	0.1941(3)	1.31(3)	1.0
O5	0.8332(7)	0.1683(3)	0.6716(4)	1.31(3)	1.0
O6	0.5020(7)	0.1714(4)	0.9429(4)	1.31(3)	1.0
$R_p = 7.7$, $R_{wp} = 9.9$, $R_{exp} = 7.2$, $R_B = 3.0$, $\chi^2 = 2.0$					

Table 2. Selected (Fe, Al–O) bond distances for $Al_{2-x}Fe_xO_3$ ($x = 0.8$, 0.9 and 1.0) as obtained from Rietveld refinements of x-ray powder diffraction data at $T = 295$ K. Numbers in parentheses are estimated statistical errors referring to the last significant digit.

	$x = 0.8$	$x = 0.9$	$x = 1.0$
Fe1–O1	2.33(1)	2.35(1)	2.332(4)
Fe1–O1	2.13(1)	2.05(1)	2.117(4)
Fe1–O2	2.08(1)	2.04(1)	2.077(4)
Fe1–O3	1.87(1)	1.88(1)	1.884(3)
Fe1–O5	1.90(1)	1.97(1)	1.940(4)
Fe1–O5	1.91(1)	1.85(1)	1.912(3)
Fe2–O1	2.22(1)	2.21(1)	2.253(4)
Fe2–O2	2.03(1)	2.03(1)	2.052(3)
Fe2–O3	1.87(1)	1.90(1)	1.901(3)
Fe2–O4	2.10(1)	2.18(1)	2.147(3)
Fe2–O5	1.84(1)	1.84(5)	1.840(3)
Fe2–O6	1.96(1)	1.98(5)	1.987(4)
Fe3–O2	1.78(1)	1.77(1)	1.777(4)
Fe3–O4	1.77(1)	1.81(1)	1.790(3)
Fe3–O6	1.74(1)	1.71(5)	1.724(4)
Fe3–O6	1.77(1)	1.79(5)	1.795(4)
Fe4–O1	1.94(1)	1.91(1)	1.951(4)
Fe4–O1	1.96(1)	2.05(1)	1.989(3)
Fe4–O2	1.94(1)	1.99(1)	1.990(4)
Fe4–O3	1.82(1)	1.82(1)	1.834(3)
Fe4–O5	1.93(1)	1.88(1)	1.937(3)
Fe4–O5	2.01(1)	1.98(1)	2.013(3)

estimated as about 1 wt%. After a few refinement circles we succeeded in obtaining a good agreement between theoretical and experimental patterns. The agreement parameters were further reduced when we left as free parameters the occupancy of the octahedral coordinated sites. This fact is related directly to the common occupancy of these sites by Fe and Al ions.

The agreement indices are further improved when the oxygen positional parameters and all the isotropic thermal parameters are incorporated into the refinement. The refined cell constants, atomic coordinates, occupancy factors and isotropic thermal parameters, and selected cation–oxygen distances deduced from Rietveld refinement, are listed in table 1 and table 2, respectively. The data for the $x = 1$ sample are in good agreement with those of Bouree *et al* [19]. At this point, we would like to comment on some interesting points based on the results of tables 1 and 2. (a) The three octahedral sites are occupied by both Fe^{3+} and Al^{3+} ions. Within the estimated standard deviations the iron occupancy in the tetrahedral site is practically zero, in agreement with the Mössbauer data (see below). For the $x = 0.8$ sample Fe^{3+} ions are distributed in octahedral Fe1 and Fe2 sites. As x increases, the iron content of Fe1 and Fe2 sites further increases and at the same time some iron starts to occupy the octahedral Fe4 site. It is interesting to note that the estimation of the iron occupancy, with Rietveld refinement, in the four available sites can be achieved due to their significant structural factor contrast. In spite of this significant contrast, the total iron amount is lower than the nominal for all samples. This problem may be related to the difficulty in estimating both temperature and occupancy factors by the x-ray diffraction data. (b) The coordination octahedra for both Fe1 and Fe2 sites are highly distorted since the Fe–O bonds are as long as 2.33(1) Å and 2.22(1) Å respectively. The coordination polyhedron of the Fe4 site is also not a rigid octahedron, but the difference between lower and maximum bond lengths is significantly less in comparison with those of Fe1 and Fe2 sites. Probably this high anisotropic coordination is related to magnetoelectric behavior. (c) The cell parameters increase with iron content, a fact arising from the difference of the ionic radius of Fe^{3+} and Al^{3+} (e.g. $R(Fe^{+3}) = 0.785$ Å and $R(Al^{+3}) = 0.675$ Å for octahedral coordination [30]).

In order to examine whether the ferrimagnetic transition induces some kind of structural change we study the crystal structure of the $x = 1$ sample using high-resolution synchrotron x-ray diffraction data from 300 K down to 5 K. Figure 3 shows the Rietveld plot of the SXRD measured at $T = 5$ K. The refinement results do not show any drastic structural change, in comparison with structural data above

Table 3. The structural parameters of AlFeO$_3$ at $T = 5$ K as determined from Rietveld refinement based on synchrotron x-ray diffraction data of the ID31 beam line of the ESRF. The space group $Pna2_1$ (No 33) was used. Numbers in parentheses are statistical errors referring to the last significant digit.

$a = 4.9832(1)$ Å, $b = 8.5558(1)$ Å, $c = 9.2491(1)$ Å					
Atom	x	y	z	B	N
Fe1	0.1844(2)	0.1518(2)	0.5815(2)	0.39(2)	0.66(1)/0.34(1)
Fe2	0.6715(2)	0.0321(1)	0.7984(2)	0.44(2)	0.67(1)/0.32(1)
Fe3	0.1733(3)	0.1539(3)	0.0000(0)	0.65(4)	0.06(1)/0.94(1)
Fe4	0.8143(2)	0.1609(1)	0.3043(3)	0.26(3)	0.18(1)/0.82(1)
O1	0.978(1)	0.3241(4)	0.4216(5)	1.06(3)	1.0
O2	0.507(1)	0.4910(4)	0.4311(4)	1.06(3)	1.0
O3	0.661(1)	1.0032(4)	0.1977(4)	1.06(3)	1.0
O4	0.144(1)	0.1646(4)	0.1956(4)	1.06(3)	1.0
O5	0.826(1)	0.1691(4)	0.6718(4)	1.06(3)	1.0
O6	0.500(1)	0.1726(4)	0.9440(4)	1.06(3)	1.0

$$R_p = 9.0, \ R_{wp} = 12.4, \ R_{exp} = 7.2, \ R_B = 5.6, \ \chi^2 = 2.8$$

the ferrimagnetic temperature, except for the expected cell constant contraction due to the lowering of the temperature. The refined structural parameters deduced from SXRD data of the $x = 1$ sample at $T = 5$ K are listed in table 3.

4. Magnetic measurements

Figure 4 shows the temperature variation of the magnetic moment per gram (m) of the Al$_{2-x}$Fe$_x$O$_3$ ($x = 0.8, 0.9$ and 1.0) samples. The size and the temperature variation of the magnetic moment indicate a ferromagnetic component, while the significant hysteresis of the measured moments during cooling and heating implies strong magnetic anisotropy. The measurements are taken after zero field cooling, applying a 100 Oe dc field, during warming (zfc branch) up to 350 K and finally measuring during cooling down to 5 K (fc branch). For the $x = 0.8$ sample, when the temperature is raised, the magnetization shows an abrupt increase at ≈ 50 K. Subsequently it forms a double-peak structure and then decreases, at the transition temperature, T_N. The corresponding fc branch increases smoothly as the temperature decreases below T_N. This strong difference between zfc and fc branches is indicative of a ferrimagnetic/ferromagnetic material with strong coercivity due to the strong uniaxial anisotropic behavior (see below). When a small magnetic field is applied at 5 K in a demagnetized sample, after zero field cooling (the domains inside a crystallite are arranged either parallel or antiparallel to the easy axis, which in turn are randomly distributed at the surface of the unit sphere), the magnetic moment parallel to the external magnetic field, H is only a small percentage of the total saturated moment. Only when the external field becomes comparable with the effective anisotropic field, $H_A = \mu_0 M(T)/2K(T)$, does appreciable magnetic moment appear. On the other hand, during the fc measurement, since the anisotropic field and accordingly the coercive field are zero at T_N, all the crystallites with a-axis (the easy magnetic axis as we discuss below) parallel to the external field contribute to the magnetic moment. The magnetic measurements clearly reveal an increase of T_N
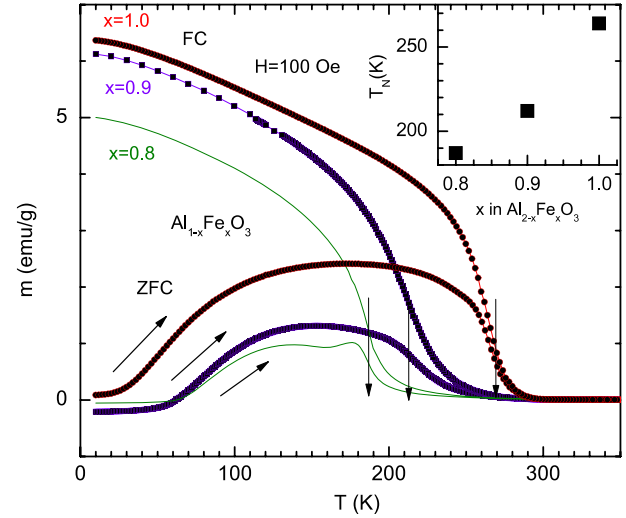

Figure 4. Temperature variation of zfc and fc magnetic moment per gram of Al$_{2-x}$Fe$_x$O$_3$ ($x = 0.8, 0.9$ and 1.0) samples. The inset shows the concentration variation of the Néel temperature, T_N. Arrows indicate the Néel temperature defined at the temperature where dm/dT displays a maximum.
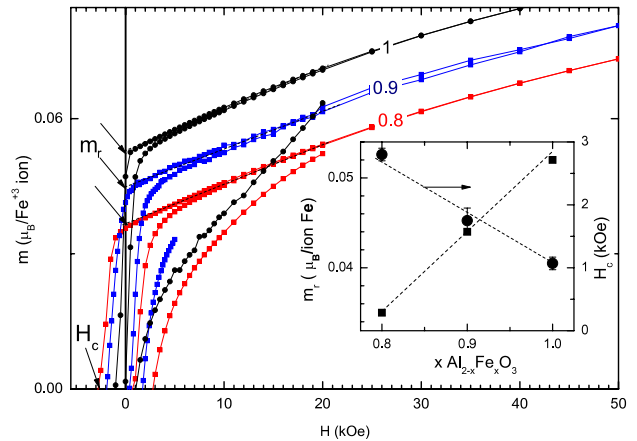

Figure 5. Isothermal magnetization hysteresis loops at $T = 5$ K of Al$_{2-x}$Fe$_x$O$_3$ ($x = 0.8, 0.9$ and 1.0) samples. The inset shows the concentration variation of the coercive field and the remanent ferromagnetic moment.

(defined at the temperature where $|dm/dT|$ shows a peak) as x increases. This increase is related to the increase of the iron occupancy firstly in the Fe4 site and secondly in Fe1 and Fe2.

Figure 5 depicts parts of the hysteresis loops of the Al$_{2-x}$Fe$_x$O$_3$ ($x = 0.8, 0.9$ and 1.0) sample at $T = 5$ K. These measurements demonstrate clearly the dependences of the remanent moment (increasing function) and coercive field (decreasing function) on x, depicted in the inset of figure 5. Similar to the behavior of T_N, the increase of the remanent moment is most probably connected with the occupancy of iron in the Fe4 site. The simultaneous increase of the iron content by the same amount, in the Fe1 and Fe2 sites, does not contribute to the remanent moment because these sublattices are coupled antiferromagnetically. Therefore, only when iron is substituted for Al by different amounts in Fe1 and Fe2
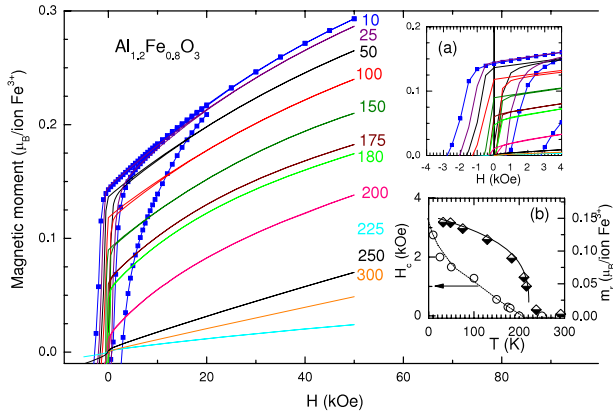
Figure 6. Magnetic field dependence of the magnetic moment at several temperatures of the $Al_{1.2}Fe_{0.8}O_3$ sample. Inset (a) shows a zoom of the measurements at zero field region, while inset (b) shows the temperature variation of the remanent moment and the coercive field. In inset (b) the solid line through the m_r data represents the equation $m_r = m_0(1 - T/T_N)^n$ (see the main text).

sites is a net ferromagnetic moment produced. The decrease of the coercive field does not have a simple explanation. In the earlier studies on the isostructural $Ga_{2-x}Fe_xO_3$ compound several reasons have been advocated to explain the origin of the large magnetic anisotropy ($H_A \sim 40$–50 kOe) [12, 17]. Levine *et al* [12], based on classical dipole energy calculations, explained satisfactorily the sign, magnitude, temperature and iron concentration dependence of H_A. On the other hand, Schelleng *et al* [17] argued that in addition to the dipolar interactions antisymmetric exchange and single-ion anisotropy contribute significantly as well.

In order to study in more detail the magnetic behavior of the orthorhombic samples we carry out isothermal magnetization loops for temperatures in the interval 5 K– 300 K. Representative experimental results are shown in figure 6 for the $x = 0.8$ sample. The virgin magnetic moment firstly increases suddenly with the magnetic field for $H < 20$ kOe and then asymptotically approaches a less abrupt increment. The reverse part follows a different path, showing a remanent magnetic moment 0.1 emu g^{-1} and zeroed at the coercive field $H_c \sim 3$ kOe. Taking into account similar measurements in single crystal and powder samples [18] of the isomorphous $Ga_{1-x}Fe_xO_3$, we conclude that the particular variation implies weak ferrimagnetic behavior with uniaxial anisotropy. The neutron diffraction data have shown [18, 19] that $AlFeO_3$ and $GaFeO_3$ adopt a collinear ferrimagnetic structure with Fe^{3+} magnetic moments parallel and antiparallel to the a-axis ($Pna2_1$ setting) of the unit cell, which also is the easy magnetic axis. The remanent moment of our powder sample is related to the a-axis remanent moment $m_r = \int_0^{\pi/2} m_a \cos\theta \sin\theta \, d\theta = m_a/2$. Using this relation we estimated the remanent moment along the a-axis, which is depicted in inset (b) of figure 6. In the same inset plotted is the temperature dependence of the coercive field. A least square fitting of the $m_r(T)$ data with a power law $m_r(T) = m_r(0)(1 - T/T_N)^n$ yields an exponent $n = 0.27 \pm 0.01$ and
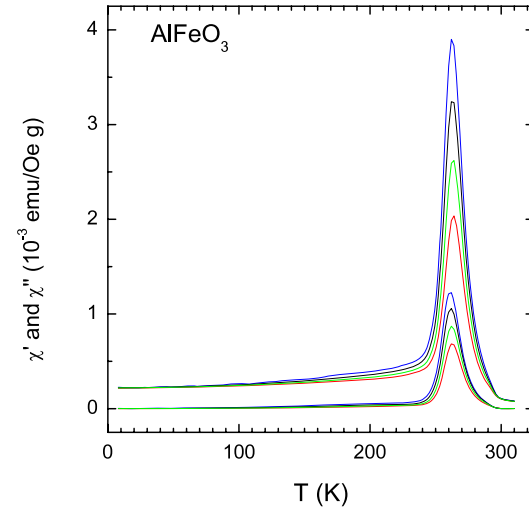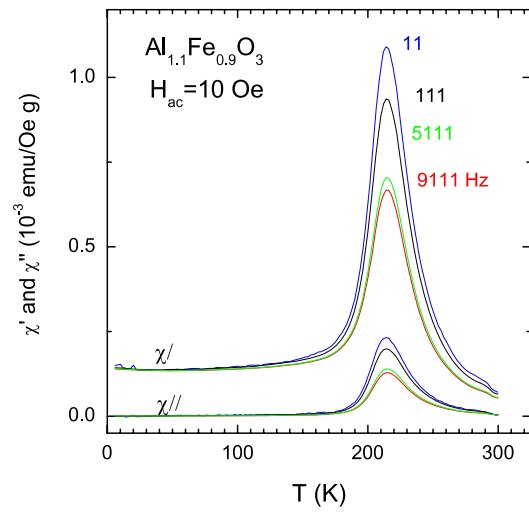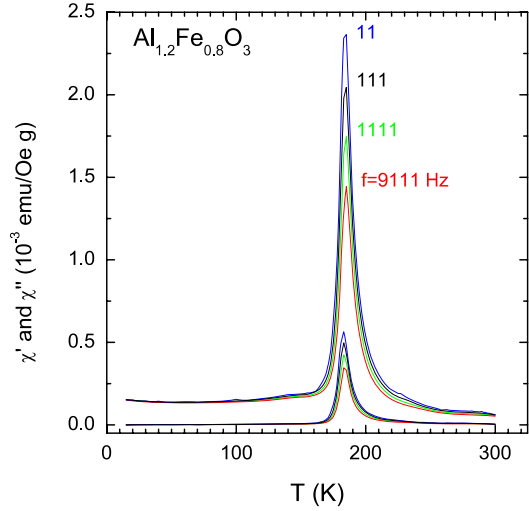

Figure 7. Temperature variation of the real, $\chi'(T)$, and imaginary, $\chi''(T)$, parts of the ac susceptibility for the $Al_{2-x}Fe_xO_3$ samples (a) $x = 0.8$, (b) $x = 0.9$ and (c) $x = 1.0$.

zero-temperature remanent moment 0.15 ± 0.01 μ_B/ion Fe^{3+}. Similar behavior has also been observed for the other samples.

Figures 7(a)–(c) show the temperature variation of the external ac susceptibility (real, $\chi'(T)$, and imaginary, $\chi''(T)$,

ac susceptibility, uncorrected for demagnetizing effects) measured under an ac magnetic field $H_{ac} = 10$ Oe at frequencies $f = 11, 111, 1111$ and 9111 Hz for $x = 0.8, 0.9$ and 1.0 samples, respectively. At $T = 185, 210$ and 260 K, for $x = 0.8, 0.9$ and 1.0, $\chi'(T)$ displays a sharp peak. The corresponding $\chi''(T)$ exhibits a sharp maximum at the temperature where $\chi'(T)$ takes the maximum value, with an amplitude comparable to $\chi'(T)$. The size and the temperature behavior of $\chi'(T)$ is different from those observed in antiferromagnetic compounds. This behavior can be explained quantitatively by considering the interaction magnetic energy of the sample's magnetic moment, M, with external magnetic field, H, and uniaxial anisotropy term $E(\theta_M) = K \sin^2 \theta_M - \mu_0 M H \cos(\theta_H - \theta_M)$. Here K is the anisotropy constant, θ_M is the angle of the magnetic moment with the easy axis, and θ_H is the angle of the external field with the easy axis. When the anisotropic field is significantly larger than the external field $H \ll H_A$ the condition for minimum $dE_{\theta_M}/d\theta_M = 0$ yields $\theta_M \approx \mu_0 M (H/H_A) \sin^2 \theta_H$. The measured magnetic moment averaged over the surface of a sphere yields $\langle M \rangle \approx (2/3)(H/H_A)M$, which subsequently yields the magnetic susceptibility $\chi = d\langle M \rangle / dH \propto M(T)/H_A(T)$. Taking into consideration the experimental observed temperature variation of $m_r(T) \propto M(T)$ and $H_A(T) \propto H_c(T)$ we can explain very well the rapid reduction of $\chi(T)$ below T_N. The divergence of χ' above T_N is related to the ferrimagnetic transition [31]. The large imaginary part around T_N for a ferrimagnet has been attributed by Skumryev *et al* [31] to the large domains arising from the weak demagnetizing field, inherent to a ferrimagnetic compound.

Finally, let us comment on the frequency dependence of the ac susceptibility in the region of the transition temperature. We can qualitatively understand this behavior supposing a single relaxation time. In this case, the magnetization under an external ac magnetic field should follow the equation $dM/dt + M/\tau = \chi_0 H_{ac} \sin(\omega t)$, where χ_0 is the dc susceptibility. Simple integration gives the frequency dependence of in and out of phase fundamental susceptibility $\chi' = \chi_0/(1 + (\omega\tau)^2)$ and $\chi'' = \chi_0(\omega\tau)/(1 + (\omega\tau)^2)$. In the regime $\omega\tau > 1$ both χ' and χ'' decrease with ω. Our data can be explained with a relaxation type behavior adopting a distribution of relaxation times.

5. Mössbauer spectra

Figure 8 shows the Mössbauer absorption spectra (MS) of the $Al_{2-x}Fe_xO_3$ compound for $x = 0.8, 0.9$ and 1.0 at 295 K consisting of two broad non-Lorentzian asymmetric peaks. The Mössbauer spectra do not exhibit a well resolved structure so as to allow for an unambiguous assignment to the crystallographic sites. Nevertheless, their intensity asymmetry, the larger line width (in comparison with a thin α-Fe absorber) and some details in the line shape prompted us that they can be modeled with three components. According to the crystal structure model for the cations there are four different crystallographic sites, three with cations in a distorted octahedral environment and one in a nearly regular tetrahedral environment. According to our crystal structure refinements
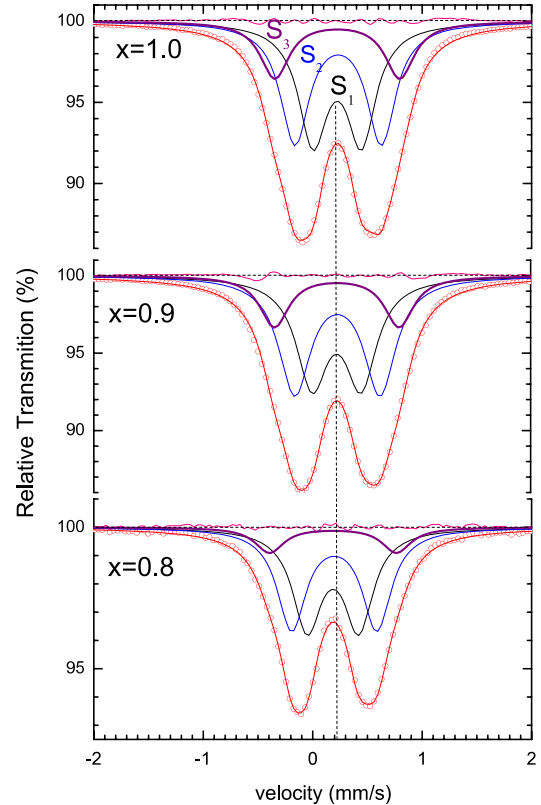

Figure 8. Mössbauer spectra of the the $Al_{2-x}Fe_xO_3$ ($x = 0.8, 0.9$ and 1) sample at $T = 295$ K fitted with three quadrupole doublets denoted S_1, S_2 and S_3, respectively.

there is no doubt that they are occupied by both iron and aluminum. For the tetrahedral site the crystallographic data cannot give an explicit answer. For $x = 0.8$ we found that iron occupancy at Fe1, Fe2 and Fe4 sites is 40%, 50% and 10%, respectively. As the iron content increases a part of the extra iron is equally distributed in Fe1 and Fe2 sites and the rest goes in the Fe4 site. Therefore, it is plausible that the paramagnetic Mössbauer spectra should consist of, at least, three paramagnetic doublets. Because our data do not show clearly the existence of different components for their analysis, we should impose certain restrictions in order for the fitting to give a reasonable result. By keeping the HWHM of the absorption lines equal with that estimated from a standard α-Fe absorber ($\Gamma/2 = 0.16$ mm s^{-1}) and by employing the Le Caer [32] method, we estimated the distribution of the quadrupole splitting. This distribution revealed that the experimental spectra can be decomposed with three nested quadrupole doublets with quadrupole splitting $\Delta_1 \approx 0.4$ mm s^{-1}, $\Delta_2 \approx 0.7$ mm s^{-1} and $\Delta_3 \approx 1.1$ mm s^{-1}. Subsequently, using this information we refined the hyperfine parameters by employing a three component fit with free parameters of their isomer shifts, quadrupole splittings and relative areas. The half widths at half maximum for all components are kept constant, $\Gamma/2 = 0.16$ mm s^{-1}. The three components used to fit the MS and the total theoretically calculated spectra are shown in figure 8 with solid lines. The final hyperfine parameters estimated with least square fitting are listed in table 4. We should note that the MS spectra can

Table 4. Hyperfine parameters of the Mössbauer paramagnetic spectra of the $Al_{1-x}Fe_xO_3$ ($x = 0.8$, 0.9 and 1.0) compound, obtained from least squares fits of the Mössbauer spectra at $T = 295$ K. $\Gamma/2$ is the half line width in mm s^{-1}, δ is the isomer shift relative to metallic Fe at RT in mm s^{-1}, $\Delta E_Q = (1/2)|e|V_{zz}Q(1 + \eta^2/3)^{1/2}$ is the quadrupole splitting and $W\%$ the relative spectra area of each doublet. The numbers in parentheses are estimated standard deviations referring to the last significant digit.

	δ	ΔE_Q	$\Gamma/2$	$W\%$
$x = 0.8$, $\chi^2 = 1.2$				
S_1	0.297(1)	0.470(2)	0.16	44(1)
S_2	0.302(1)	0.778(1)	0.16	45(2)
S_3	0.291(3)	1.158(6)	0.16	11(1)
$x = 0.9$, $\chi^2 = 5.5$				
S_1	0.328(1)	0.428(1)	0.16	38(1)
S_2	0.335(1)	0.792(1)	0.16	44(1)
S_3	0.327(1)	1.188(5)	0.16	18(1)
$x = 1.0$, $\chi^2 = 6.5$				
S_1	0.339(1)	0.440(1)	0.16	40(1)
S_2	0.338(1)	1.002(1)	0.16	41(1)
S_3	0.330(1)	1.352(1)	0.16	19(1)

also be fitted with two doublets, using higher $\Gamma/2$ or crossed doublets with quite different isomer shifts. However, the higher χ^2, in comparison with the three doublet model and the lack of correspondence to crystallographic data, led us to reject this model. The values of the estimated isomer shift for all doublets indicate that the iron is in the Fe^{3+} valence state. Based on the data listed in table 4, it is reasonable to attribute the S_1 and S_2 components to iron occupying the Fe1 and Fe2 sites, while S_3 to Fe4. The particular assignment is based on the correlation of the relative abundance of S_i with iron occupancy estimated from Rietveld refinements. It is expected that the two components arising from Fe1 and Fe2 sites have nearly equal areas, while the spectrum area of iron from the Fe4 site increases with x.

At this point we would like to note that our MS show that iron does not occupy the Fe3, tetrahedral site. This is an important experimental conclusion that can only be arrived at with the help of the Mössbauer spectroscopy. In the literature, it is well known that high spin trivalent iron, in a tetrahedral oxygen environment, has significantly lower isomer shift with respect to the octahedral one, due to the higher covalency bonding. For example, in iron substituted β-Ga_2O_3 at room temperature the MS consist of two paramagnetic doublets [11] with different isomer shifts ($\delta_T \approx 0.17$ mm s^{-1} and $\delta_O \approx 0.35$ mm s^{-1}) attributed to iron occupying the tetrahedral and octahedral sites of β-Ga_2O_3, respectively. Similarly, in yttrium iron garnet $Y_3Fe_5O_{12}$, where tetrahedral and octahedral sites exist, the isomer shift of tetrahedral iron is lower than that of the octahedral [33]. Consequently, the absence of any paramagnetic component with low isomer shift led us to conclude that iron does not occupy the tetrahedral Fe3 sites. In order to support further our site assignment, we performed theoretical calculations of the quadrupole spitting for sites Fe1, Fe2 and Fe4, employing the point charge approximation

using our refined crystal structure data. For the Fe_i sites we assumed that they are occupied by point charge with charge $3|q_e|$. This is a good approximation, at least for high spin ferric iron ions, since the spherical symmetry of the ^6S ground state is preserved inside the crystal field, zeroing then the valence contribution in the electric field gradient tensor. Performing lattice sums inside a $100a \times 100b \times 100c$ parallelepiped, we calculated the electric field gradient tensor and subsequently the quadrupole splitting using the relation $\Delta E_Q = (1/2)q_e^2 Q(1 - \gamma)|V_{zz}|(1 + \eta^2/3)^{1/2}$. $\gamma = -9.1$ is the Sternheimer antishielding factor [34] of Fe, V_{zz} is the maximum eigenvalue of the V_{ij}, $\eta = (V_{yy} - V_{xx})/V_{zz}$ is the asymmetry parameter, $Q = 0.21 \times 10^{-24}$ cm^2 is the quadrupole moment [35] of ^{57}Fe and q_e is the charge of a proton. We should note that Q values range within 0.08–0.21 b. $Q = 0.21$ b is preferred, and its use would approximately double the predicted Δ with respect to $Q = 0.08$ b. The theoretically estimated quadrupole splittings for the compound $x = 1$ are $\Delta(Fe1) = 0.27$ mm s^{-1}, $\eta = 0.75\Delta(Fe2) = 0.46$ mm s^{-1}, $\eta = 0.46$, and $\Delta(Fe3) = 0.57$ mm s^{-1}, $\eta = 0.47$. These values differ from the observed ones by a factor of two, but we can consider them as an indication that we have analyzed the spectra correctly.

Room temperature Mössbauer spectra for $Al_{2-x}Fe_xO_3$ and isostructural $Ga_{2-x}Fe_xO_3$ compounds have been reported in the past by several groups [9–11, 13, 18]. In the case of $Ga_{2-x}Fe_xO_3$ ($x = 0.8$) two doublets have been observed [11, 13, 18] with nearly equal isomer shifts ($\delta \approx 0.35$ mm s^{-1} relative to α-iron at room temperature) and $\Delta E_Q \approx 0.49$ mm s^{-1}, and $\Delta E_Q \approx 1.05$ mm s^{-1} for the more intense and less intense, respectively. These authors have attributed the doublet with lower ΔE_Q to octahedral Fe^{3+}, while that with higher ΔE_Q to Fe^{3+}, which occupies the tetrahedral sites. For $Al_{2-x}Fe_xO_3$ Mössbauer spectra have been reported only for the $x = 1$ sample [10], in good agreement with our results.

Figures 9–11 show the temperature evolution of the MS for all samples. As the temperature becomes lower than the Néel temperature (estimated from magnetization or ac-susceptibility data), the MS exhibit magnetic splitting due to non-zero hyperfine magnetic field originating from long range ferrimagnetic order. We should note that the MS in the close vicinity of the Néel temperature display a mixed structure consisting of paramagnetic and magnetically split sub-spectra. This situation is quite common in magnetic oxides when the magnetic sites are commonly occupied by two or more ions.

Let us discuss the $T = 4.2$ K spectra. We attempted to fit these spectra using one magnetic component. The main features of the spectra could be reproduced with hyperfine parameters $\delta = 0.468(4)$ mm s^{-1}, $H = 473$ kOe and $\epsilon = (3/2)(3\cos^2\Theta - 1 + \eta\sin^2\Theta\cos 2\Phi)e^2Q/12 = -0.099(1)$ mm s^{-1}. However, characteristic discrepancies between the experimental and theoretical spectra were observed, indicating that this simplistic model could not account for the observations. On the other hand, it is obvious that the observed spectrum does not have the appropriate resolution in order to discern three distinct components (sextets), in accordance with the paramagnetic and crystal
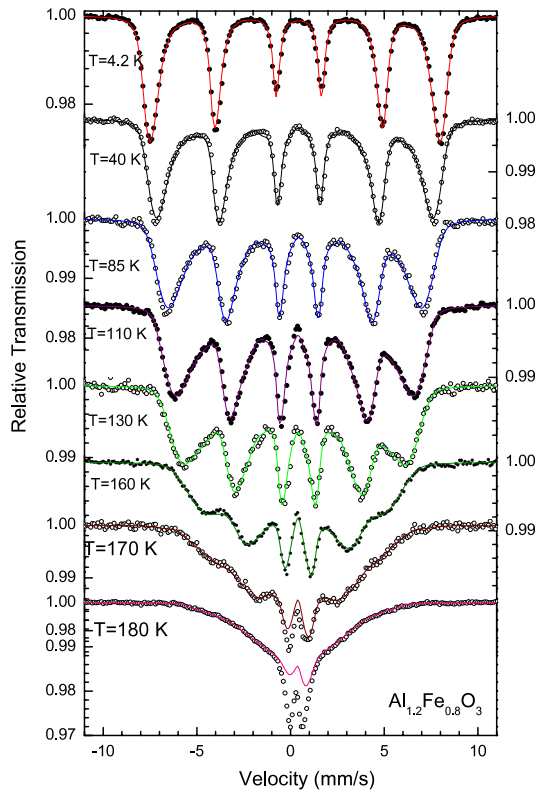
Figure 9. Mössbauer spectra of the $Al_{1.2}Fe_{0.8}O_3$ sample at several temperatures. The symbols represent the experimental spectra. Lines through symbols are theoretical spectra calculated with the Le Caer method.

Figure 10. Mössbauer spectra of the $Al_{1.1}Fe_{0.9}O_3$ sample at several temperatures. The symbols represent the experimental spectra. Lines through symbols are theoretical spectra calculated with the Le Caer method.

structure data. The broad character of the absorption lines does not allow an unbiased analysis with several sites, therefore we decided to use the Le Caer method in fitting the magnetic spectra. With Le Caer's method we can deconvolute a magnetically split Mössbauer spectrum, supposing that it is the result of the convolution with a hyperfine field distribution. If the iron ions occupy crystallographic sites without static or dynamic disorder the distribution of the hyperfine field should be narrow peaks. In our case diamagnetic Al atoms occupying together with iron the three octahedral sites produce large static fluctuations in the hyperfine fields, hence giving rise to broad distributions of the hyperfine magnetic field.

Figures 12–14 show the hyperfine field distributions as estimated by the Le Caer method. The particular analysis has been based on the following simplified assumptions. We supposed that all the magnetic components have the same isomer shift (depending on temperature) and a temperature independent quadrupole splitting ($\varepsilon \approx -0.11$ mm s^{-1}). In the insets of figures 12–14 we depict the temperature variation of the most probable hyperfine field (H_p located at the maximum of the $P(H_{hyp})$) the max value and the lower limit of the hyperfine field distribution. H_p follows the power law $H_p = H_0(1 - T/T_N)^n$. The solid lines through the experimental points represent least square fittings yielding the parameters $H_0 = 495$ kOe and $n = 0.27 \pm 0.01$ for all samples. The particular temperature dependence is related to the second order ferrimagnetic to paramagnetic phase transition, in agreement with our magnetic measurements.
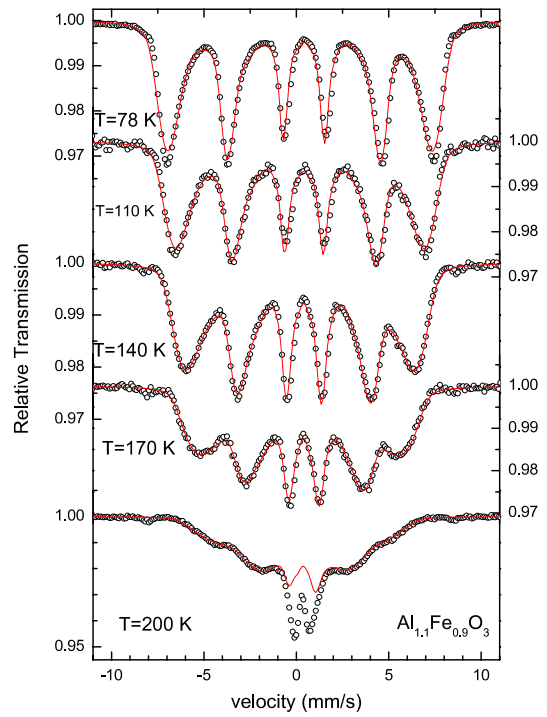

Figure 11. Mössbauer spectra of the $AlFeO_3$ sample at several temperatures. The symbols represent the experimental spectra. Lines through symbols are theoretical spectra calculated with the Le Caer method.
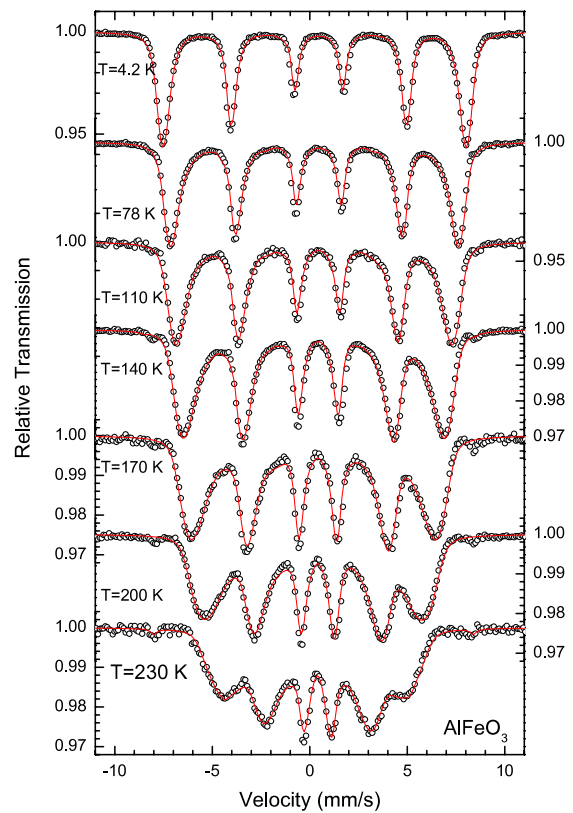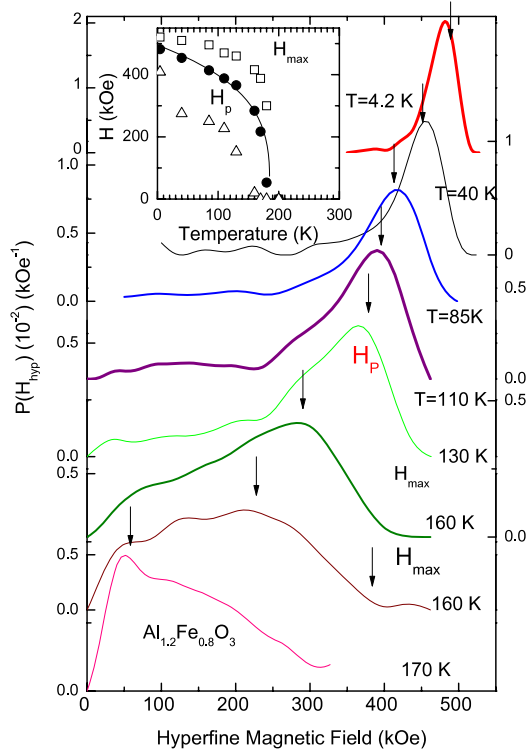
Figure 12. Hyperfine field distributions for the $Al_{1.2}Fe_{0.8}O_3$ sample, estimated with the Le Caer method. The inset shows the temperature dependence of the most probable field and the upper and lower bounds of the hyperfine field distribution. The dotted lines are guides to the eye. The solid line represents the equation $H_p(T) = H_0(1 - T/T_N)^n$ (see the text).

Figure 13. Hyperfine field distributions for the $Al_{1.1}Fe_{0.9}O_3$ sample, estimated with the Le Caer method. The inset shows the temperature dependence of the most probable field and the upper and lower bounds of the hyperfine field distribution. The dotted lines are guides to the eye. The solid line represents the equation $H_p(T) = H_0(1 - T/T_N)^n$ (see the text).

Having estimated the hyperfine magnetic field distribution we are able to comment on several interesting issues. The first concerns the value of $H_p \sim 490$ kOe at 4.2 K in comparison with that observed in rare earth perovskite orthoferrites (≈ 550 kOe), where each octahedrally coordinated Fe^{3+} is antiferromagnetically coupled with the six nearest Fe^{3+} neighbors through an oxygen anion. In a sample in a magnetically ordered state, the magnetic hyperfine field $H_{hf}(T)$ measured via the line splitting in Mössbauer spectra is equal to the difference of the 'up' and 'down' spin densities at the nucleus $H_{hf} = \Psi_s^\uparrow - \Psi_s^\downarrow$ [36]. Sawatzky *et al* [36] have shown that the hyperfine magnetic field is given by

$$\mathbf{H}_{hf}(T) = \mathbf{H}_{Free} + \mathbf{H}_{COV} + \mathbf{H}_{STHF}.$$

The three terms correspond to free ion (Free), covalence correction (COV) and supertransferred hyperfine field (STHF) contributions, respectively. A large number of studies indicate that the free ion and covalence contribution to hyperfine field is $\mathbf{H}_{FREE} + \mathbf{H}_{COV} \approx -450\widehat{\mathbf{S}}$ kOe. Here $\widehat{\mathbf{S}}$ is the unit vector along the thermal average electronic spin. In the STHF only the magnetic nearest neighbor cations $\mathbf{H}_{STHF} = \sum B_n \widehat{\mathbf{S}}$ (the sum concerns only magnetic nearest neighbors) contribute. The constants B_n are positive scalar quantities, associated with the nearest neighbor bond lengths and angles, and can be expressed as a function of the Fe–O–Fe bond angles θ_n, through the relation $B_n = H_\pi + (H_\sigma - H_\pi)\cos^2 \theta_n$ [33, 36].
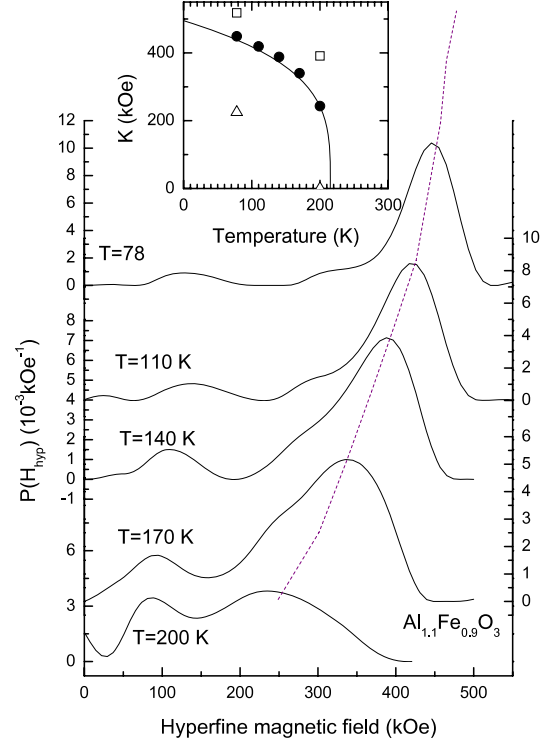
In this equation the parameters $H_{\pi,\sigma}$ represent quantitatively the 'overlap distortions of the Fe cation s orbitals caused by the ligand p orbitals having been unpaired by spin transfer via π and σ bonds into unoccupied 3d orbitals on the NN cations n' [33, 36]. As it has been pointed out [33], especially in amorphous yttrium garnets, the width of the hyperfine field distribution is directly related to the STHF through the distribution of the B_n parameters. In our case the fluctuating part in the hyperfine field arises from the STHF due to the stochastic nature of the nearest neighbors (magnetic Fe, non-magnetic Al). Taking into account the nearest neighbors' bond angles and the magnetic structure (see figure 1), the values of the STHF can explain the low values of the magnetic hyperfine field at 5 K. Theoretical calculations of Sawatzky *et al* [33, 36] have shown that B_n can take values as high as $B_n \approx -20$ kOe. A ferromagnetic (antiferromagnetic) Fe–O–Fe bond produces a positive(negative) supertransferred field, respectively. In the $Al_{2-x}Fe_xO_3$ compound we need to take into consideration only the strong antiferromagnetic superexchange interactions which concern only iron ions occupying Fe1, Fe2 and Fe4 sites, especially the strong $\sim 180°$ Fe1–O–Fe2 and Fe1–O–Fe4 superexchange antiferromagnetic interactions. The coupling inside Fe1 and (Fe2, Fe4) layers is ferromagnetic with a bond angle near 90°, leading to negligible STHF. Obviously, the STHF is zero also when an iron ion is connected with an aluminum ion. Consequently, on average, the mean supertransferred field should be directly related to
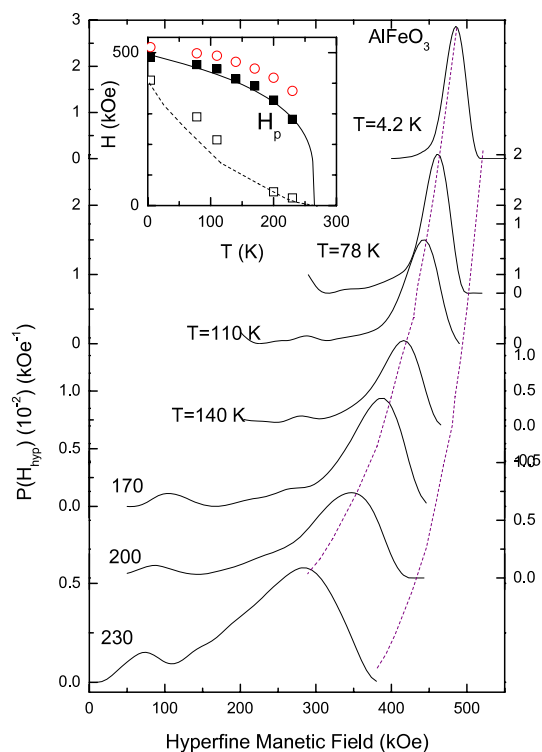
Figure 14. Hyperfine field distributions for the AlFeO$_3$ sample, estimated with the Le Caer method. The inset shows the temperature dependence of the most probable field and the upper and lower bounds of the hyperfine field distribution. The dotted lines are guides to the eye. The solid line represents the equation $H_p(T) = H_0(1 - T/T_N)^n$ (see the text).

the probability that both cations in a $\sim 180°$ Fe1–O–(Fe2, Fe4) bond are Fe^{3+}. When both ions are Fe^{3+} ions one expects the maximum HSHF $H_{STHF} = 2 \times 20$ kOe, which in turn gives a total hyperfine field $H_{hf}(T) \approx 490$ kOe, in good agreement with the experimental results.

Finally, let us comment on the temperature dependence of the hyperfine field distributions. At zero temperature the width of the distributions is narrow and the existing width should be accounted for by the fluctuations due to the STHM field induced by the presence of the non-magnetic aluminum. Our experimentally estimated hyperfine field distributions show a strong temperature dependence as temperature increases. Essentially, for $T > T_N/2$ the hyperfine field measured at the iron nucleus takes values from zero up to the value expected for a typical variation of the iron spin in a magnetically ordered state. As the temperature increases, the iron magnetic moment loses the site 'identity'. The particular behavior has been observed in several studies related to the magnetic system where the magnetic site is occupied from several magnetic and/or non-magnetic ions. In a typical ferromagnetic or antiferromagnetic compound, one expects a power law variation of the hyperfine magnetic field $H \sim (1 - T/T_c)^n$, with roughly temperature independent line width (implying a delta type distribution of the H_{hyp}). For this kind of compound the fluctuations of the electronic spins are related to spin wave excitations, which, however, are too fast in comparison with the Larmor frequency, averaged on the scale of the Larmor

period. These types of fluctuations reduce the mean value of the electronic spin. It is interesting to note that the neutron diffraction data of Bouree [19] and Bertaut [18] clearly show a long range order of the iron magnetic moment. Therefore, it is reasonable to ask why we observe this strange temperature variation of the hyperfine field distributions. The particular behavior can be explained considering the localized excitation of the magnetic moments produced by the presence of the non-magnetic aluminum. In a disordered system, except the spin wave excitations, there are localized excitations that concern change of the spin states with local character confined in the region of few sites. These types of excitation in combination with the extended ones produce this complicated behavior.

In conclusion, we have studied the Al$_{2-x}$Fe$_x$O$_3$ ($x = 0.8, 0.9$ and 1) compound by using x-ray diffraction, magnetization and Mössbauer spectroscopy techniques. The magnetic measurements show magnetic transitions at $T_N = 180, 210$ and 260 K for $x = 0.8, 0.9$ and 1.0 respectively, that can be attributed to a transition from the ferrimagnetic to the paramagnetic state. The paramagnetic Mössbauer spectra can be analyzed by three quadrupole doublets associated with the octahedral Fe1, Fe2 and Fe4 sites. The values of the hyperfine parameters show that iron ions are in the Fe^{3+} high spin state. The spectrum area of the doublet with larger quadrupole splitting increases with x, and in combination with the x-ray diffraction result, it is attributed to the iron which occupies the Fe4 site. The magnetically split spectra at $T = 4.2$ K consist of a six line spectrum with broad lines, indicative for a distribution of the hyperfine magnetic field $P(H_{hyp})$. Analysis of crystallographic data, magnetic measurements and Mössbauer results revealed that the magnetic properties of Al$_{2-x}$Fe$_x$O$_3$ are influenced by both the iron occupancies in Fe4 and (Fe1, Fe2) sites.

Acknowledgments

References

[1] Smolenkii G A and Chupis I E 1982 *Sov. Phys.—Usp.* **25** 475
[2] Hill N A 2000 *J. Phys. Chem.* B **104** 6694
[3] Efremov D V, Van Den Brink J and Khomskii D I 2004 *Nat. Mater.* **3** 853
[4] Landau L D and Lifschitz E M 1984 *Electrodynamics of Continuous Media* 2nd edn (Oxford: Pergamon)
[5] Richardson H M, Ball F and Rigby G R 1952 *Trans. Intern. Ceramic. Congr. 3rd Congr. (Paris)* p 173
[6] Muan A 1958 *Am. J. Sci.* **256** 413
[7] Dayal R R, Gard J A and Glasser F P 1965 *Acta Crystallogr.* **18** 574
[8] Remeika J P 1960 *J. Appl. Phys.* **31** 2635
[9] Frankel R B, Blum N A, Foner S, Freeman A J and Schieber M 1965 *Phys. Rev. Lett.* **15** 958
[10] Trooster J M 1965 *Phys. Lett.* **16** 21
[11] Trooster J M and Dynanus A 1967 *Phys. Status Solidi* **24** 487

[12] Levine B F, Nowlin C H and Jones R V 1968 *Phys. Rev.* **174** 174

[13] Mackenzie K J D and Brown I W M 1984 *J. Mater. Sci. Lett.* **3** 159

[14] Dweck J 1968 *Phys. Rev.* **168** 602

[15] Pinto A 1966 *J. Appl. Phys.* **37** 4372

[16] Nowlin C H and Jones R V 1963 *J. Appl. Phys.* **34** 1262

[17] Schelleng J H and Rado G T 1969 *Phys. Rev.* **179** 541

[18] Bertaut E F, Bassi G, Buisson G, Chappert J, Delapalme A, Pauthenet R, Rebouillat H P and Aleonard R 1966 *J. Physique* **27** 433

[19] Bouree F, Baudour J L, Elbadraoui E, Musso J, Laurent C and Rousset A 1996 *Acta Crystallogr.* B **52** 217

[20] Devaux X, Rousset A, Broto J M, Rakoto H and Askenazy S 1990 *J. Mater. Sci. Lett.* **9** 371

[21] Kida N, Kaneko Y, He J P, Matsubara M, Sato H, Akoh H and Tokura Y 2006 *Phys. Rev. Lett.* **96** 167202

[22] Kim J-Y, Koo T Y and Park J-H 2006 *Phys. Rev. Lett.* **96** 047205

[23] Arina T *et al* 2004 *Phys. Rev.* B **70** 064426

[24] Popov Yu F *et al* 1998 *JETP* **87** 146

[25] Kimura T, Goto T, Shintani H, Ishizaka K, Arima T and Tokura Y 2003 *Nature* **426** 55

[26] Abrahams S C, Reddy J M and Bernstein J L 1965 *J. Chem. Phys.* **42** 3957

[27] Rodriguez-Carvajal J 1993 *Physica* B **192** 55

[28] Finger L W, Cox D E and Jephcoat A P 1994 *J. Appl. Crystallogr.* **27** 892

[29] Stephens P W 1999 *J. Appl. Crystallogr.* **32** 281

[30] Shannon R D 1976 *Acta Crystallogr.* A **32** 751

[31] Skumryev V, Ott F, Coey J M D, Anane A, Renard J-P, Pinsard-Gaudart L and Revcolevschi A 1999 *Eur. Phys. J.* B **11** 401

[32] Le Caer G and Dubois J M 1979 *J. Phys.* E **12** 1083

[33] Lines M E and Eibschütz M 1984 *Phys. Rev.* B **30** 1416

[34] Sternheimer R M 1963 *Phys. Rev.* **130** 1423

[35] McNab T K and Barrett P H 1971 *Mössbauer Effect Methodology* vol 7, ed I J Gruverman (New York: Plenum) p 59

[36] Sawatzky G A and Van der Woude F 1974 *J. Physique* **12** C6–47